Food Chemistry 493 (2025) 145901

Contents lists available at ScienceDirect

Food Chemistry

journal homepage: www.elsevier.com/locate/foodchem

Facile all-in-one detection of nitrofurantoin in feed and milk by magnetic separation assisted differential pulse voltammetry

Xingdong Yang [a], Wan-yue Zhuang [a], Sen Zhang [a], Jie Zou [b], Aiguo Gu [b], Qi Wang [b], Jun-qin Qiao [a], Hong-zhen Lian [a,*]

[a] State Key Laboratory of Analytical Chemistry for Life Science, School of Chemistry & Chemical Engineering and Centre of Materials Analysis, Nanjing University, Nanjing 210023, China
[b] Jiangsu Product Quality Testing and Inspection Institute, Nanjing 210007, China

ARTICLE INFO

Keywords:
Nitrofurantoin
Feed
Milk
Magnetic solid-phase extraction
Co/N-doped carbon
Electrochemical detection

ABSTRACT

Nitrofurantoin (NFT) residue in animal-derived food poses a threat to human health. We proposed a novel strategy for NFT determination in feed and milk, which connected pretreatment technology to electrochemical detection. Cobalt nanoparticles encapsulated in nitrogen-doped carbon nanostructure with carbon nanotubes (Co/N-CNS-CNTs) were prepared for modifying magnetic electrodes. Meanwhile, magnetic reduced graphene oxide wrapped in phenyl-functionalized mesoporous silica (MG@mSiO_2-Phe) was synthesized as magnetic solid-phase extraction (MSPE) adsorbent. The modified magnetic electrode can gather NFT-adsorbed MSPE materials and then detect NFT via differential pulse voltammetry (DPV) without elution and solution transfer procedures. Both analyte enrichment by MG@mSiO_2-Phe and signal amplification by Co/N-CNS-CNTs synergistically improved detection sensitivity with slope of calibration curve and limit of detection of 1.365 μA (μmol L^{-1})$^{-1}$ and 6 nmol L^{-1}, respectively. In actual samples, this method exhibits higher accuracy and reliability compared with direct DPV detection, and simpler operation process compared with liquid-chromatography method.

1. Introduction

Nitrofurantoin (NFT), as a member of the nitrofuran drugs, is synthetic broad-spectrum antibiotic and mainly used to treat urinary system infections clinically (Liu et al., 2007). Because various antibiotics are proved to have growth-promoting effects at sub-therapeutic levels (Zhu et al., 2023), NFT was used as a growth promoter and a feed additive in animal husbandry (Zhang, Lai, et al., 2020). The accumulation of NFT residue in foodstuffs of animal origin as well as in environment can produce short-term adverse effects on humans such as diarrhea, pruritus, dizziness, etc., and potentially lead to the emergence of antibiotic-resistant genes and resistant bacteria (Kokulnathan & Chen, 2020). The use of NFT has been strictly banned for animal-derived food in many countries and regions including the European Union, the United States, Australia, etc. (Khong et al., 2004; Li et al., 2017). In 2019, the Ministry of Agriculture and Rural Affairs of China also issued an announcement prohibiting the use of NFT in food-producing animals (The Ministry of Agriculture and Rural Affairs of China, 2019). Therefore, it is necessary to develop an effective, accurate and sensitive method for determination of NFT in animal feed or animal-derived food samples in order to protect the food safety and public health.

In national and industrial standards of China, the chromatography coupled with different detection systems is still the most common method for NFT due to its high reliability and wide acceptance, as well as in Foods Program Compendium of Analytical Methods of the U.S. Food and Drug Administration (FDA) (Entry-Exit Inspection & Quarantine Industrial Standard of China, 2013; FDA Food Program Compendiun of Analytical Laboratory Methods, 2019; National Standard of China, 2008). However, liquid chromatography tandem mass spectrometry (LC-MS) method always requires sophisticated instrumentation, well-trained personnel and long analysis time. In addition, the sample pretreatment procedure is laborious, time-consuming and organic reagents-consuming (Arancibia et al., 2003; Kaufmann et al., 2015), which cannot meet the requirement for rapid, on-site and real-time detection of NFT. Currently, electrochemical approaches have been exploited for the detection of NFT owing to the advantages of

* Corresponding author at: School of Chemistry & Chemical Engineering and Center of Materials Analysis, Nanjing University, 163 Xianlin Avenue, Nanjing 210023, China.
E-mail address: hzlian@nju.edu.cn (H.-z. Lian).

https://doi.org/10.1016/j.foodchem.2025.145901
Received 15 November 2024; Received in revised form 17 July 2025; Accepted 9 August 2025
Available online 11 August 2025

simple equipment requirement, rapid response, easy operation and low cost, in which some advanced electrode modification materials have been prepared for the signal amplification including carbon-based nanomaterials, metal and metal oxide nanomaterials, conducting polymer, framework nanomaterials and composite nanomaterials (Miao et al., 2025). When electroanalytical methods are applied to actual samples, a matrix dilution operation is often adopted with the aim of circumventing matrix interference in the signal detection (Sivaraman et al., 2023; Zhang, Zhu, et al., 2020). However, the matrix dilution would assuredly reduce the concentrations of targets and detection rates, leading to the false-negative results (Stahnke et al., 2012; Yang et al., 2015). Therefore, the development of simple, suitable and non-diluting pretreatment technology equipping on the electroanalytical approach is necessary.

In terms of pretreatment technology, solid-phase extraction (SPE) is the most commonly used in chromatography-based methods for separating and enriching target analytes, but the cumbersome operation in conventional SPE procedure makes it mismatching for rapid electrochemical detection (Liu et al., 2022; Yang et al., 2024; Yu et al., 2022). Magnetic solid-phase extraction (MSPE), combining SPE with magnetic separation, is a kind of new dispersive SPE technology using an external magnet to achieve the separation of targets and matrix, which greatly improves extraction efficiency and simplifies operation process (Xie et al., 2023; Zhang, Li, et al., 2023). It can be seen that MSPE is a simple, rapid and electrochemical detection-adaptable sample pretreatment technology. However, the elution procedure of target analytes from the adsorbents increases the effort of sample pretreatment, and probable incomplete elution causes the loss of the analytes. The elution-free detection of the adsorbed analytes on the MSPE adsorbents by suitable technique is a promising solution to resolve the shortages. Li research group combined MSPE with surface-enhanced Raman spectroscopy (SERS) for sulfonamides determination in aquatic products using magnetic $Ti_3C_2T_x/Fe_3O_4/Ag$ as MSPE adsorbent and SERS substrate without elution procedure prior to detection (Yu et al., 2022). Instead, the $Ti_3C_2T_x/Fe_3O_4/Ag$ adsorbing phthalic sulfathiazole and silver sulfadiazine was separated magnetically from the sample solution and then redispersed in water, and the re-constructed dispersion solution was finally dipped onto a silica wafer for SERS detection. For electrochemical detection, more conveniently, the MSPE adsorbents carrying analytes can be directly attracted onto the surface of a magnetic electrode from sample solution, and subsequently the analytes be in-situ detected on the electrode. Our research group previously developed magnetic $CoFe_2O_4$/graphene coated with C_{18}-functionalized mesoporous silica as MSPE adsorbent for separation and enrichment of promethazine, followed by DPV detection on nitrogen-doped hollow carbon microspheres modified magnetic glassy carbon electrode (MGCE) not only without elution procedure but also without solution transfer procedure (Yang et al., 2024). In fact, the magnetic electrode was also used as the MSPE magnet to build an all-in-one MSPE-electroanalysis strategy. However, there have been very few reports that MSPE technology is combined with electrochemical detection via magnetic electrode for rapid determination of pharmaceutical, veterinary drug and pesticide residues in feed and food samples.

Herein, we developed a new method integrating the MSPE pretreatment technology and electrochemical detection for the determination of NFT in complex feed and milk samples. The electrocatalyst of cobalt nanoparticles (Co NPs) encapsulated in nitrogen-doped carbon nanostructure with abundant carbon nanotubes (Co/N-CNS-CNTs) was prepared via the pyrolysis of bimetallic Zn/Co zeolitic imidazolate frameworks (ZIFs) for the modification of electrode towards electrochemical detection of NFT in DPV. Meanwhile, the MSPE materials for NFT separation and enrichment were prepared by wrapping the magnetic reduced graphene oxide (MRGO) with phenyl-functionalized hybrid mesoporous silica (MG@mSiO_2-Phe). The NFT-adsorbed magnetic materials were easily gathered on the surface of the modified electrode for NFT detection without additional magnet for MSPE. Both the analyte enrichment by MG@mSiO_2-Phe and the signal amplification by Co_5/N-CNS-CNTs would improve the performance of NFT detection. The hyphenated MSPE-DPV protocol was applied to the detection of NFT in actual samples including cattle and sheep feed and skimmed milk.

2. Experimental section

2.1. Materials and chemicals

NFT, flutamide (Flu), *N*-methyl-4-nitroaniline (MNA), chloramphenicol (Cap), metronidazole (Mtz), $Zn(NO_3)_2{\cdot}6H_2O$, $Co(NO_3)_2{\cdot}6H_2O$, 2-methylimidazole (2-MI) Nafion solution, ciprofloxacin (Cip), amoxicillin (Amo), nitrofurazone (Nfz) and furazolidone (Fzd) were purchased from Shanghai Macklin Biochemical Co., Ltd. (Shanghai, China). Graphene oxide (GO) and oxytetracycline (Otc) were obtained from Shanghai Yuanye Bio-Technology Co., Ltd. (Shanghai, China). $FeCl_3{\cdot}6H_2O$, ethylene glycol and polyethylene glycol-20,000 were purchased from Tianjin Heowns Biochem Technologies Co., Ltd. (Tianjin, China). Tetraethyl orthosilicate (TEOS), phenyl triethoxysilane (PTES), cetyltrimethyl ammonium bromide (CTAB) and nilutamide (Nlt) were supplied by Aladdin Biochemical Technology Co., Ltd. (Shanghai, China). Ultrapure water was prepared by Milli-Q system (resistivity >18.25 MΩ•cm). The 0.1 mol L^{-1} PBS (pH 7.0) was prepared by mixing 61.5 % 0.1 mol L^{-1} K_2HPO_4 and 38.5 % 0.1 mol L^{-1} KH_2PO_4. For other pH values (5.0, 6.0, 8.0, and 9.0), the 0.1 mol L^{-1} PBS was prepared by varying the mixing ratio of these two solutions. The electrolyte (pH 7.0) was 0.1 mol L^{-1} PBS containing 0.1 mol L^{-1} KCl prepared by mixing 0.1 mol L^{-1} K_2HPO_4 + KCl and 0.1 mol L^{-1} KH_2PO_4 + KCl. MGCE (Φ = 3 mm), Ag/AgCl (in saturated KCl) electrode and platinum column electrode were supplied by Wuhan Gaoss Union Technologies Co., Ltd. (Wuhan, China). The cattle and sheep feed was purchased online from feed factory, and skimmed milk was purchased from a local supermarket in Nanjing, China.

2.2. Apparatus

A CHI660E electrochemistry workstation (Chenhua, Shanghai, China) equipped with a conventional three-electrode system was utilized to perform all electrochemical measurements, in which a modified MGCE was used as working electrode, a Ag/AgCl (in saturated KCl) as reference electrode and a platinum column as counter electrode. All the NFT adsorption experiments were monitored using a UV–Vis absorption spectrophotometer (NanoDrop2000, ThermoFisher, USA). The morphology and microstructure of synthetic MG@mSiO_2-Phe and Co/N-CNS-CNTs were visualized by a scanning electron microscope (JSM-7800F, JEOL, Japan) and a transmission electron microscope (Tecnai G2 F20 S-TWIN, FEI, USA). The crystal structure of MG@mSiO_2-Phe and Co/N-CNS-CNTs was characterized by a powder X-ray diffractometer (Bruker D8 Advance, Bruker, German) equipped with Cu Kα radiation. The information of functional groups of MG@mSiO_2-Phe was collected by a Fourier transform infrared spectrometer (Nicolet-6700, Nicolet, USA). Raman spectra of MG@mSiO_2-Phe and Co/N-CNS-CNTs were collected by a laser confocal Raman spectrometer (Renishaw inVia-Reflex, Renishaw, UK). The surface area and pore size of mesoporous MG@mSiO_2-Phe and Co/N-CNS-CNTs were measured by a N_2 adsorption-desorption instrument (BELSORP MaxII, MicrotracBEL, Japan). The magnetic characterization of MG@mSiO_2-Phe was carried out with a vibrating sample magnetometer (Lakeshore-7404, Lakeshore, USA) at 300 K. The surface elemental composition of MG@mSiO_2-Phe and Co/N-CNS-CNTs was studied by an X-ray photoelectron spectroscope (ESCALAB Xi+, ThermoFisher, USA). The comparative experiments for the NFT determination in feed and milk samples were performed on a high performance liquid chromatograph (LC-20AD, Shimadzu, Japan) with a UV–Vis spectrophotometric detector. The chromatographic column used was Welch Ultimate XB-C_{18} column (4.6 × 250 mm i.d., 5 μm, Welch, China). SPE cartridge used was Doprah™

MCX (60 mg/3 mL, Welch, China).

2.3. Synthesis of Co/N-CNS-CNTs

Scheme 1A illustrates the synthesis process of the Co/N-CNS-CNTs. The bimetallic Zn/Co-ZIFs were first prepared with reference to the preparation of monometallic ZIF-67 by Xia et al. (Xia et al., 2016). In the synthesis of Zn_1/Co_5-ZIFs, 1 mmol (0.298 g) $Zn(NO_3)_2{\cdot}6H_2O$ and 5 mmol (1.455 g) $Co(NO_3)_2{\cdot}6H_2O$ were dissolved in a mixed solution of 20 mL methanol and 20 mL ethanol as solution A. 24 mmol (1.97 g) 2-MI was dissolved in another mixed solution of 20 mL methanol and 20 mL ethanol as solution B. The solutions A and B were then mixed under continuous stirring for 10 s, and the final solution was kept statically in a flask for 20 h at room temperature. After the resultant suspension was centrifugated (10,000 rpm) for 10 min, the purple precipitates were collected, washed in ethanol three times, and dried at 50 °C. Other bimetallic ZIFs were also obtained using the same procedure, except for the use of different molar ratios of $Zn(NO_3)_2{\cdot}6H_2O/Co(NO_3)_2{\cdot}6H_2O$ (6/0 for Zn_6/Co_0-ZIFs, 5/1 for Zn_5/Co_1-ZIFs, 3/3 for Zn_3/Co_3-ZIFs, and 0/6 for Zn_0/Co_6-ZIFs). The as-synthesized Zn_1/Co_5-ZIFs as well as other ZIFs were spread in a ceramic boat, heated to 350 °C at a heating rate of 2 °C min^{-1} and then maintained for 1.5 h in a tube furnace. The temperature was further raised to 800 °C at the same heating rate and then kept for 3.5 h. The furnace was under Ar/H_2 flow (9/1, *V/V*) during the pyrolysis process. After cooling down naturally, the obtained black powdery product was collected and donated as Co_5/N-CNS-CNTs, and other products as Co_0/N-CNS, Co_1/N-CNS-CNTs, Co_3/N-CNS-CNTs and Co_6/N-CNS-CNTs, respectively.

2.4. Construction of Co/N-CNS-CNTs modified electrode

The MGCE can be dismantled after every electrochemical test in order to facilitate the removal of magnetic materials on the electrode surface. The electrode cleaning procedure followed the previous literature (Zhu et al., 2013). In brief, the MGCE was polished with alumina slurry, and rinsed thoroughly with ultrapure water and ethanol. Afterwards, the electrode surface was vigorously blown dry by N_2 gas flow. The electrocatalyst suspension was prepared by dispersing 1 mg Co_5/N-CNS-CNTs in 1 mL ultrapure water containing 20 μL of 5 wt% Nafion solution, followed by ultrasonication for 60 min. The clean MGCE

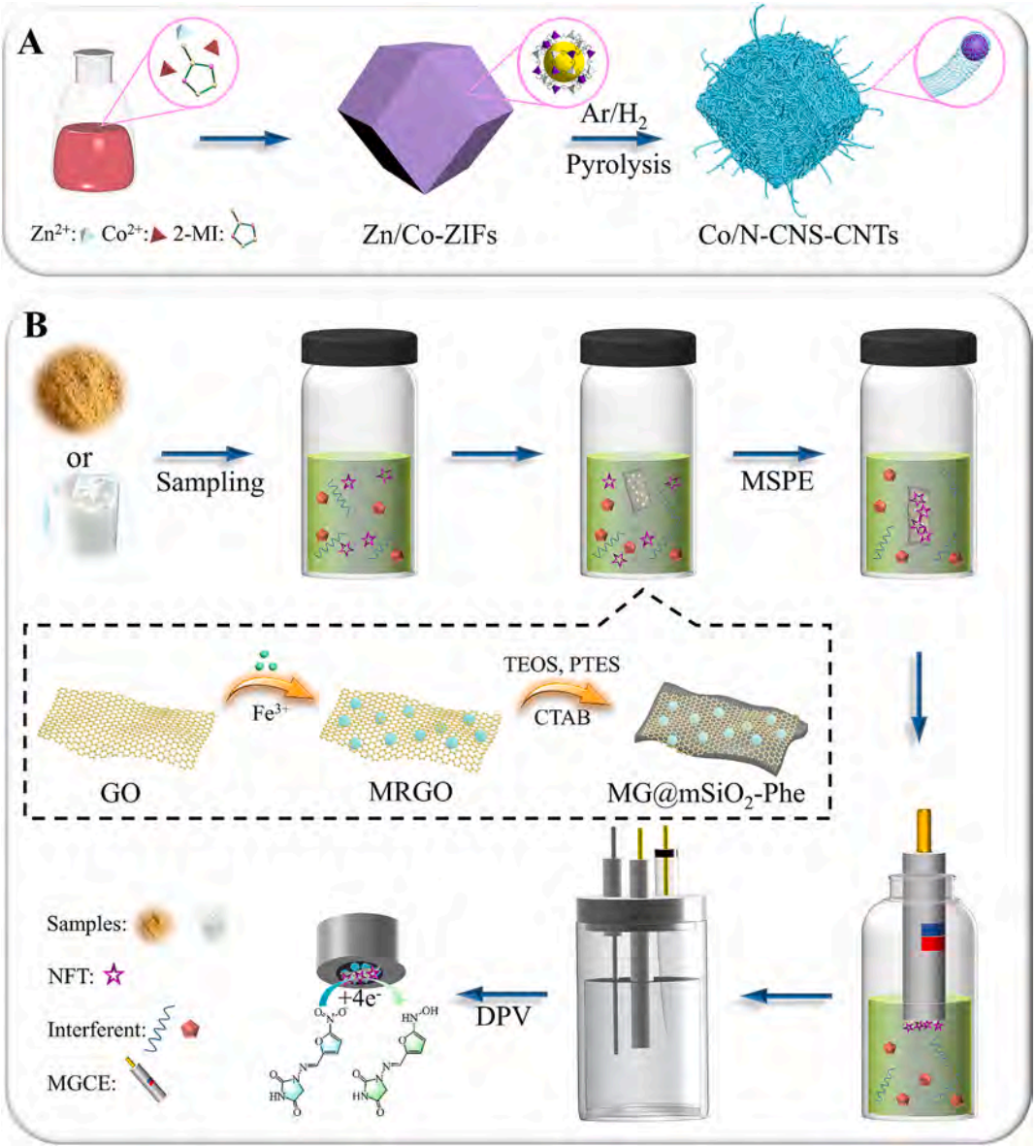

Scheme 1. (A) The synthesis process of the Co/N-CNS-CNTs. (B) The schematic illustration of MSPE-DPV hyphenated method for electrochemical detection of NFT.

surface was cast by 7 μL Co_5/N-CNS-CNTs suspension, and then dried at room temperature for more than 5 h to obtain the Co_5/N-CNS-CNTs modified electrode. Other electrocatalyst modified electrodes were also constructed by respectively casting the suspension including Co_0/N-CNS, Co_1/N-CNS-CNTs, Co_3/N-CNS-CNTs and Co_6/N-CNS-CNTs.

2.5. Synthesis of MG@mSiO$_2$-Phe for MSPE

The MRGO was prepared based on solvothermal method referring to our earlier work (Yang et al., 2024), and the schematic procedure is shown in dashed box of Scheme 1B. Firstly, 150 mg GO, 405 mg $FeCl_3 \cdot 6H_2O$, 150 mg trisodium citrate, 1.8 g sodium acetate and 1 g polyethylene glycol-20,000 were dispersed in 40 mL ethylene glycol in a centrifuge tube. The mixed suspension was ultrasonicated and stirred for 1 h, respectively. Subsequently, the above mixture was transferred into a Teflon-lined stainless-steel autoclave and hydrothermally treated at 200 °C for 10 h. After the autoclave was cooled down, the products were washed thoroughly three times with ethanol and dried at 50 °C in a vacuum oven.

The prepared MRGO was wrapped with a layer of hybrid mesoporous silica with phenyl groups based on a surfactant-mediated sol-gel method. In detail, 50 mg MRGO and 500 mg CTAB were dispersed in 50 mL ultrapure water, and ultrasonically treated for 10 min. Then, dilute NaOH solution was mixed with the above suspension to maintain a final NaOH concentration of 1 mmol L^{-1}, and ultrasonically treated for 10 min again. The above mixture was transferred into a three-necked round-bottom flask, and stirred at 60 °C for 30 min, and then 2.5 mL TEOS/ethanol (1/4, *V/V*) solution was added dropwise to the flask in 30 min. Subsequently, 150 μL TEOS/PTES (2/1, *V/V*) solution was injected into the flask for reaction at 60 °C of 12 h. The resulting products were collected by a magnet and washed thoroughly three times with ultrapure water. After the residual CTAB was completely removed by a Soxhlet extraction experiment in acetone for 24 h, the MG@mSiO$_2$-Phe nanocomposites were dried at 50 °C in a vacuum oven.

2.6. MSPE and DPV detection of NFT

The workflow for MSPE enrichment and DPV detection of NFT is drawn in Scheme 1B. Firstly, 10 mg MG@mSiO$_2$-Phe was suspended in 10 mL ultrapure water. Prior to each using, a 1-min ultrasonication process was carried out to disperse the nanocomposites uniformly. Then, 250 μL of the suspension were mixed with 20 mL of NFT solution at different concentrations in 0.1 mol L^{-1} PBS, and the suspension was vortexed for 20 min. The prepared Co_5/N-CNS-CNTs modified electrode was immersed into above mixture to drive the NFT-adsorbed magnetic nanocomposites to be attached onto the modified electrode surface. Afterwards, the electrode was gently taken out and immersed into the electrolytic cell containing 10 mL electrolyte solution (pH 7.0). The electrode loading NFT-adsorbed magnetic nanocomposites was electrochemically measured by DPV without elution of NFT, which was performed by scanning the potential from 0 to −0.8 V with an incremental potential of 4 mV, and a pulse amplitude of 50 mV.

2.7. Preparation of actual samples for NFT detection

For DPV detection of NFT, the sample pretreatment of cattle and sheep feed samples was carried out mainly according to an entry-exit inspection & quarantine industrial standard method of China (Entry-Exit Inspection & Quarantine Industrial Standard of China, 2013) with simplification. Feed sample was vigorously ground to powders in a mortar. The powders (6.0 g) were weighted, fortified with a certain amount of standard NFT and placed in 40 mL acetonitrile in a centrifuge tube. The mixture was vortexed for 1 min and ultrasonicated for 15 min. The supernatant was collected by centrifugation at 3800 rpm for 15 min, and then transferred to a flask. The supernatant was evaporated to dryness under reduced pressure at 40 °C, and the residues on the wall of the flask were dissolved in 40 mL 0.1 mol L^{-1} PBS (pH 7.0) for later MSPE and DPV detection of NFT. The direct DPV detection of NFT in feed without MSPE was carried out for comparison. In this experiment, NFT in feed samples was extracted by acetonitrile and then evaporated as above, with the difference that the residues were dissolved in the electrolyte solution without MSPE procedure. Finally, the Co_5/N-CNS-CNTs modified electrode was immersed into the electrolyte solution for the direct detection of NFT by DPV. The skimmed milk was processed according to a simplified national standard method of China (National Standard of China, 2008). 8.0 mL skimmed milk and a certain amount of standard NFT were mixed with 40 mL 0.5 mol L^{-1} trichloroacetic acid in a centrifuge tube, and then the mixture was ultrasonicated, vortexed and shaken respectively for 5 min. Afterwards, the supernatant was collected by centrifugation at 10000 rpm for 10 min. A suitable amount of NaOH solution was added to adjust the pH of the supernatant to 7.0, and it was then fixed in 50 mL using ultrapure water. This neutral solution was used for later MSPE and DPV detection of NFT. In the direct DPV detection, the mixture of skimmed milk and trichloroacetic acid was centrifugated. Then the pH of the supernatant was adjusted and the volume was fixed as above. NFT in this neutral sample solution could not be detected by DPV on the Co_5/N-CNS-CNTs modified electrode without MSPE probably due to the medium interference by high concentration of trichloroacetic acid, so the sample solution was diluted 10 times. Finally, the modified electrode was immersed into the above diluted solution for the direct detection of NFT by DPV.

The pretreatment of cattle and sheep feed and skimmed milk samples using SPE cartridge and detection of NFT using high performance liquid-chromatography (HPLC) for comparison referred to the ref. (Entry-Exit Inspection & Quarantine Industrial Standard of China, 2013) in combination of the ref. (National Standard of China, 2008). The powders (6.0 g) of ground feed sample were weighted, fortified with a certain amount of standard NFT and placed in 40 mL acetonitrile. The mixture was vortexed for 1 min and ultrasonicated for 15 min. The supernatant was collected by centrifugation at 3800 rpm for 15 min, and then transferred to a flask. The supernatant was evaporated to dryness under reduced pressure at 40 °C, and the residues on the wall of the flask were dissolved in 40 mL H_3PO_4 solution (pH 4.0). The sample solution was purified using a MCX-SPE cartridge as follows: (1) 5 mL methanol and 5 mL H_3PO_4 solution (pH 4.0) were sequentially used to activate the SPE cartridge; (2) 4 mL sample solution passed through the prepared SPE cartridge at 1–2 mL min^{-1}; (3) 5 mL 0.1 mol L^{-1} HCl solution was used to rinse nonspecific adsorbed impurities in SPE cartridge; (4) 4 mL methanol and 4 mL methanol/ammonium hydroxide (95/5, *V/V*) were sequentially used to elute the adsorbed NFT on the cartridge. The effluent was collected, blown dry under a stream of N_2 and re-dissolved in 1 mL acetonitrile/water/DMF mixture solution (25/70/5, *V/V/V*). Then, the above solution was filtered through a 0.45 μm organic phase membrane filter for HPLC analysis on the C_{18} reversed-phase chromatographic column. The mobile phase was composed of 0.055 % H_3PO_4 solution (A) and acetonitrile (B), with the volume ratio of A and B of 9:1. The duration of isocratic elution was 20 min at a flow rate of 1 mL min^{-1}, the injection volume was 20 μL, the column temperature was 40 °C, and the UV–Vis detection wavelength was 370 nm. In the SPE-HPLC analysis for the skimmed milk samples, 8.0 mL milk sample fortified with a certain amount NFT was mixed with 40 mL acetonitrile. The mixed solution was vortexed for 1 min and ultrasonicated for 15 min. Afterwards, the supernatant was collected by centrifugation at 10000 rpm for 10 min. The NFT-containing extraction solution was subsequently treated according to the cattle and sheep feed treatment procedure.

3. Results and discussion

3.1. Characterization of the Co/N-CNS-CNTs

The bimetallic Zn/Co-ZIFs were synthesized based on their similar

topological structures, which were confirmed by scanning electron microscopy (SEM) and X-ray diffractometry (XRD). Fig. 1A shows well-defined rhombic dodecahedral structures of Zn_1/Co_5-ZIFs, and ZIFs' images of other Zn^{2+}/Co^{2+} molar ratios are shown in Fig. S1 (Supporting information) with sizes increase from ~140 to ~750 nm as the molar ratios decrease. The color of the obtained ZIFs gradually changes from white to purple indicating the increased proportion of Co^{2+} ion. XRD patterns of all ZIFs match well with simulated Zn-ZIFs and Co-ZIFs owing to their similar unit cells and crystal lattices (Fig. S2, Supporting information). Then the Co_5/N-CNS-CNTs catalyst with CNTs structure was obtained after the pyrolysis treatment of Zn_1/Co_5-ZIFs. Fig. 1B shows a SEM image of the Co_5/N-CNS-CNTs. The size and polyhedral shape of the precursor ZIFs are well retained, while the surface becomes rough and collapses. The magnified SEM image (Fig. 1C) confirms the formation of CNTs along the surface of Co_5/N-CNS-CNTs. During the thermal treatment, Co^{2+} ions were firstly reduced into metallic Co that nucleated and grew to tiny nanocrystals. Then, CNTs grew from the 2-MI as carbon source, which was catalyzed by the in-situ formed Co NPs (Dou et al., 2016). In Fig. S3 (Supporting information), Co_0/N-CNS pyrolyzed from Zn_6/Co_0-ZIFs does not contain Co NPs and CNTs. With increasing the proportion of Co^{2+} ions in the precursor ZIFs, the prepared catalysts have more and more CNTs. However, Co_6/N-CNS-CNTs does not contain a significant amount of CNTs structure, and the embedded Co NPs in Co_6/N-CNS-CNTs are large (~50 nm) in size. It is due to the fact that relatively high content of Co^{2+} in Zn_0/Co_6-ZIFs precursor sinters into large Co NPs, which have weak catalytic capacity in pyrolysis and therefore cannot catalyze the forming of CNTs. The microstructure was further investigated by transmission electron microscopy (TEM) (Fig. 1D-F). Abundant CNTs with a diameter around 15 nm grow uniformly surrounding the surface of the Co_5/N-CNS-CNTs, and the Co NPs are encapsulated by a few layered carbon shells, especially at the tip of the CNTs. Furthermore, the high-resolution TEM (HRTEM) image reveals that these thick multi-walled CNTs are crystalline. The lattice fringes with an inter-planar distance of 0.36 nm correspond to the graphitic C (002) plane (Xia et al., 2016). And the Co NPs show the crystalline lattice with the spacing of 0.20 nm, which is in good agreement with the (111) plane of face-centered cubic Co (Chen et al., 2015). Abundant edges of CNTs exposed on the surface and the tiny Co NPs would be beneficial to the synergistically enhanced electrocatalytic properties. The selected area electron diffraction (SAED) (Fig. 1G) indicates that the major diffraction rings match well with the Co NPs and CNTs, respectively (Wang et al., 2023). High-angle annular dark-field scanning TEM (HAADF-STEM) image and energy dispersive X-ray spectrometry (EDS) elemental mapping (Fig. 1H) reveal the distribution of C, N and Co elements over the Co_5/N-CNS-CNTs.

The crystalline structure of the prepared Co_5/N-CNS-CNTs was further confirmed by XRD in Fig. 1I and Fig. S4 (Supporting information). The peak at 26.2° corresponds to the (002) plane of graphitic carbon, and the other peaks at 44.3°, 51.5° and 75.8° are attributed to Co NPs (PDF No. 15–0806). Other electrocatalysts from ZIFs with different Zn^{2+}/Co^{2+} molar ratios possess the peaks of graphitic carbon and metallic Co except the Co_0/N-CNS. The diffraction peaks of Co NPs enhance with increasing the proportion of Co^{2+} ions in precursor ZIFs, and the degree of graphitization also shows gradual enhancement. Raman spectra of the electrocatalysts reveal the characteristic D and G bands of carbon (Fig. S5, Supporting information). The lower I_D/I_G value of the electrocatalysts with increasing the proportion of Co^{2+} ions in precursor ZIFs further confirms the enhancement of graphitization degree. X-ray photoelectron spectroscopy (XPS) was employed to investigate the chemical composition and elemental status of Co_5/N-CNS-CNTs electrocatalyst. The survey of XPS spectrum (Fig. 2A) reveals that the electrocatalyst is mainly composed of C, O, N and Co elements. For Co 2p

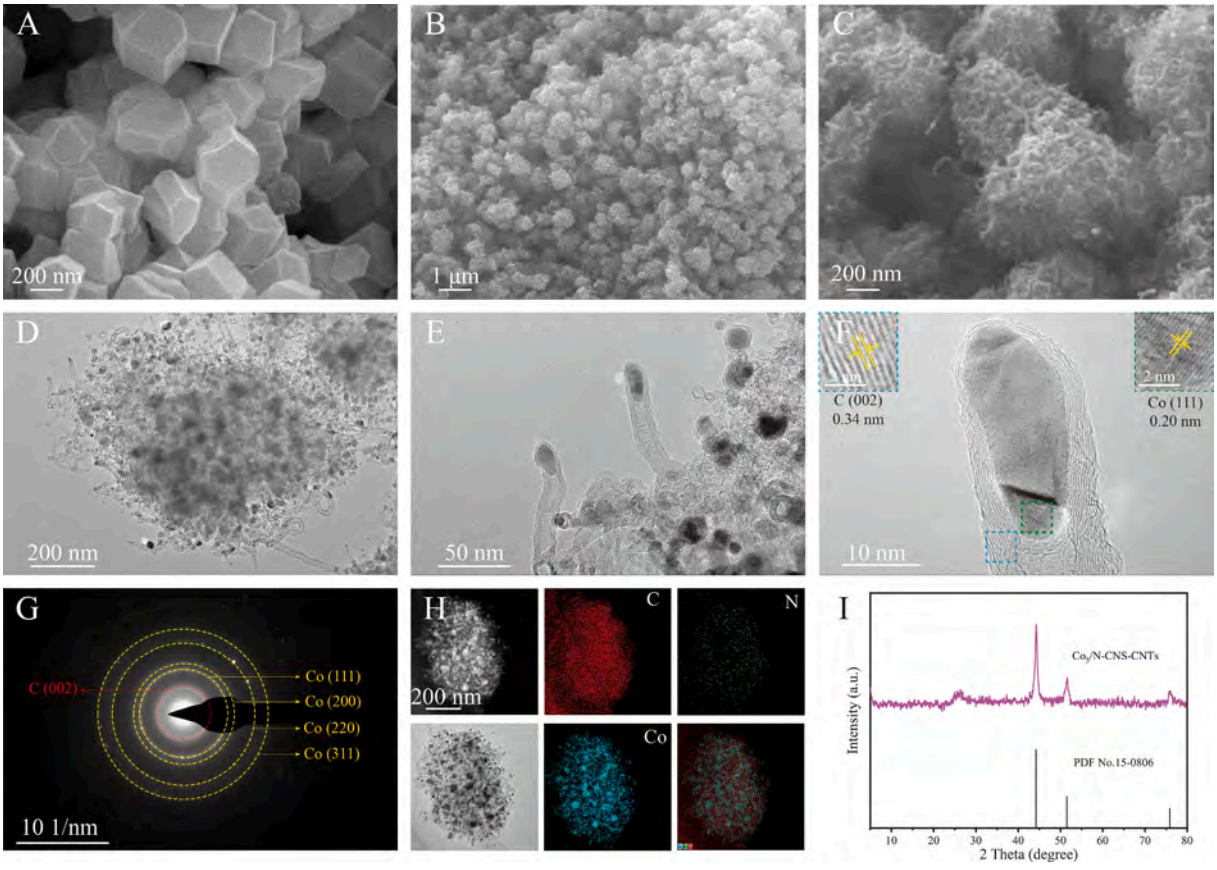

Fig. 1. (A) SEM image of Zn_1/Co_5-ZIFs. (B, C) SEM, (D, E) TEM, (F) HRTEM, (G) SAED, (H) HAADF-STEM and EDS elemental mapping and (I) XRD pattern of Co_5/N-CNS-CNTs.

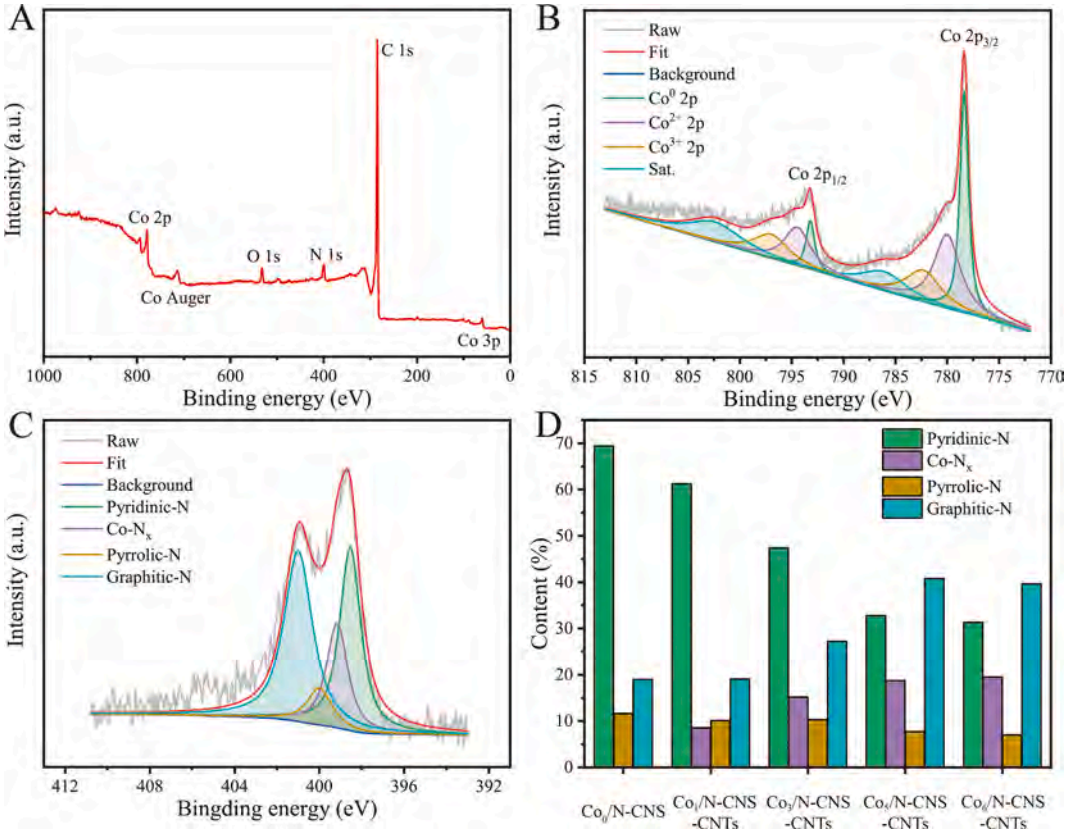

Fig. 2. (A) XPS survey, (B) Co 2p and (C) N 1 s high-resolution spectra of Co_5/N-CNS-CNTs. (D) The relative content of different N species in all electrocatalysts.

high-resolution spectrum, the characteristic peak at 778.3 eV is attributed to the Co^0 $2p_{3/2}$ (Fig. 2B). Additionally, the characteristic peaks of Co^{2+} $2p_{3/2}$ (780.1 eV) and Co^{3+} $2p_{3/2}$ (782.5 eV) are observed due to the formation of Co-N_x coordination structure and/or the surface oxidation (Wang et al., 2017). The C 1 s spectrum (Fig. S6, Supporting information) was deconvoluted into three peaks at 284.8, 285.9, and 287.1 eV, which are ascribed to C—C, C═N and C–O/C=O, respectively (Sun et al., 2021). By considering that N sites are always taken as the primarily active sites in carbon catalysts, N 1 s spectra of all electrocatalysts were deconvoluted into four peaks at 398.5, 399.1, 400.1and 401.0 eV respectively corresponding to pyridinic N, Co-N_x, pyrrolic N and graphitic N (Fig. 2C and S7, Supporting information) (Ma, Wang, Fan, et al., 2018; Song et al., 2017). By comparing the existing level of each type of N species in all electrocatalysts, the relative contents of pyridinic N and pyrrolic N have obvious decrease from Co_0/N-CNS to Co_6/N-CNS-CNTs, while that of graphitic N and Co-N_x increase, and the highest graphitic N content is in Co_5/N-CNS-CNTs (Fig. 2D). The graphitic N can accelerate the electron flow from neighbored carbon networks, and Co-N_x always plays an important role in the excellent electrocatalytic activity (Ma, Wang, Fan, et al., 2018). The Brunauer-Emmett-Teller (BET) surface area of Co_5/N-CNS-CNTs was counted as 300.4 m^2 g^{-1}. Combined with the analysis of N_2 adsorption-desorption isotherms (Fig. S8, Supporting information), the BET surface area shows a decreasing trend with increasing the proportion of Co^{2+} ions in precursor ZIFs attributed to the fact that the introduced Zn can be evaporated during pyrolysis to form the porous structure. In a word, the Co_5/N-CNS-CNTs with hierarchical structure, abundant CNTs, and the highest content of graphitic N was identified as the optimal candidate for the electrochemical catalysis of NFT at the electrode.

3.2. Electrochemical characterization of Co/N-CNS-CNTs modified electrodes

Cyclic voltammetry (CV) and electrochemical impedance spectroscopy (EIS) were carried out in 0.1 mol L^{-1} KCl solution containing 5 mmol L^{-1} $[Fe(CN)_6]^{3-/4-}$ to investigate the electrical conductivity and charge transfer resistance of the five modified electrodes. Fig. 3A shows that the electrical conductivity of bare MGCE (blue line) is well improved after the modification of Co_5/N-CNS-CNTs (red line), and the modified MGCE displays a lower peak potential. The electrochemical active surface area of Co_5/N-CNS-CNTs modified MGCE was calculated as 0.119 cm^2 by the Randles-Sevcik equation (Ma, Wang, Xie, et al., 2018) in CV test at various scan rates (Fig. S9, Supporting information), which is 56.6 % higher than the bare MGCE (0.076 cm^2). The R_{ct} values for MGCE and modified MGCE in Nyquist plots were calculated as 444 and 18.5 Ω, respectively (Fig. 3B). Among all the electrodes modified by electrocatalyst, Co_5/N-CNS-CNTs modified MGCE shows the biggest peak current and the lowest R_{ct} value (Fig. S10, Supporting information). These results of electrochemical measurement reveal that Co_5/N-CNS-CNTs is equipped with enhanced catalytic activity and excellent electrical conductivity, and has the best performance compared with other electrocatalysts.

3.3. Characterization of MSPE material MG@mSiO$_2$-Phe

The separation and enrichment of NFT from matrix were implemented by MSPE using MG@mSiO$_2$-Phe as the adsorbent. In the TEM images of prepared MG@mSiO$_2$-Phe (Fig. 4A and B), the images of typical two-dimensional (2D) nanosheets of graphene with wrinkles are observed, and the 100–150 nm Fe_3O_4 particles are anchored onto graphene. Furthermore, the translucent mesoporous silica layer with a thickness of 40–50 nm can be seen in an enlarged image (Fig. 4C), and the dense vertical pore channels with a diameter of ~3.5 nm are also

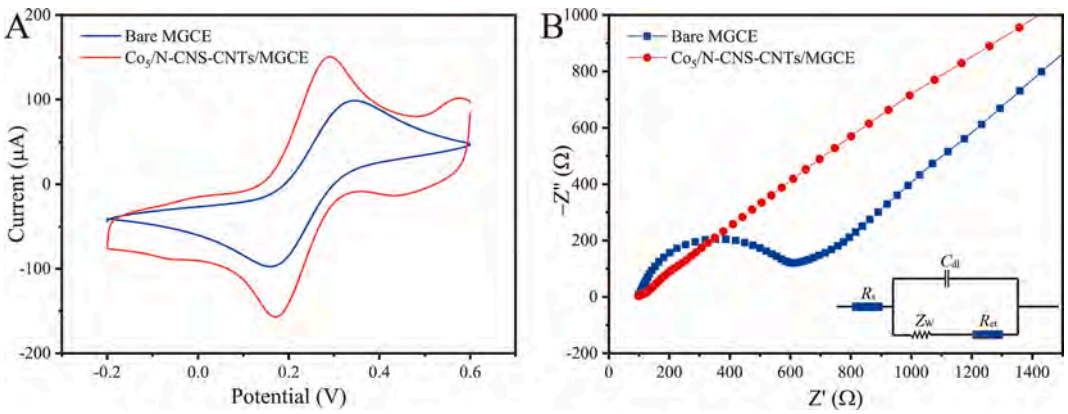

Fig. 3. (A) CV and (B) EIS in 0.1 mol L^{-1} KCl solution containing 5 mmol L^{-1} (1:1) $[Fe(CN)_6]^{3-/4-}$ acquired from bare MGCE and Co_5/N-CNS-CNTs/MGCE.

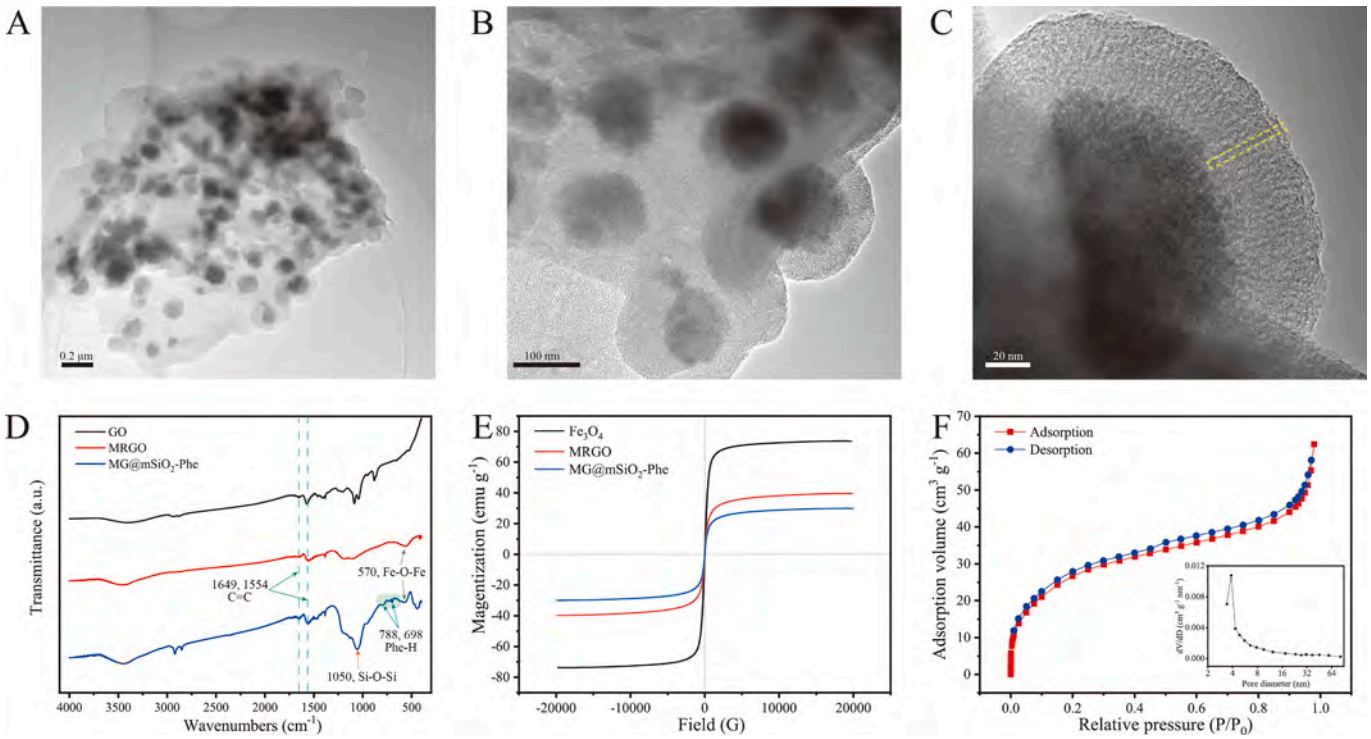

Fig. 4. (A-C) TEM images of MG@mSiO$_2$-Phe. (D) FT-IR spectra of GO, MRGO and MG@mSiO$_2$-Phe. (E) Magnetization curves of Fe_3O_4, MRGO and MG@mSiO$_2$-Phe. (F) N_2 adsorption-desorption isotherm of MG@mSiO$_2$-Phe.

observed in the dashed box, which is favorable to the capacity of adsorption. The EDS elemental mapping of MG@mSiO$_2$-Phe (Fig. S11, Supporting information) reveals that the elements of C, O and Si are homogeneously distributed on the nanocomposites, while Fe is distributed in clusters.

Fourier transform infrared (FT-IR) spectroscopy was used to confirm the phenyl modification in MG@mSiO$_2$-Phe (Fig. 4D, blue line). The newly formed peak of 570 cm^{-1} in red line (MRGO) and blue line (MG@mSiO$_2$-Phe) than black line (GO) is originated from Fe–O–Fe vibration of Fe_3O_4 nanoparticles. The peaks of 1554 and 1649 cm^{-1} are attributed to the vibrations of C═C in GO. Moreover, the broad peak around 1050 cm^{-1} corresponds to the vibration of Si–O–Si in organic-inorganic hybrid mesoporous silica layer of MG@mSiO$_2$-Phe. The two peaks of 698 and 788 cm^{-1} are ascribed to out-of-plane bending vibration of = C–H in phenyl (Feng et al., 2018). Furthermore, the characteristic D and G bands of carbon are observed at 1340 and 1598 cm^{-1} in the Raman spectra of GO, MRGO and MG@mSiO$_2$-Phe (Fig. S12, Supporting information), with the I_D/I_G values of 1.18, 1.31 and 1.28, respectively. The increasing I_D/I_G value from GO to MRGO indicates the increase of surface defects due to the hydrothermal treatment (Zhang, Zhao, et al., 2023). In XRD patterns of MRGO and MG@mSiO$_2$-Phe (Fig. S13, Supporting information), the peaks at 30.1°, 35.4°, 43.1°, 53.4°, 56.9° and 62.5° correspond to the (220), (311), (400), (422), (511) and (440) planes of Fe_3O_4 (PDF#19–0629), respectively, and the broad peak at 22° to the lattice plane (002) of RGO (Jeong et al., 2008), which is ascribed to the partial reduction of GO in hydrothermal reaction and the restoration of π-π conjugation system (Zhou et al., 2023). The XPS survey of the MG@mSiO$_2$-Phe (Fig. S14, Supporting information) indicates the existence of C, O, Fe and Si elements. The C 1 s spectrum was deconvoluted into three peaks at 284.8, 286.3 and 287.9 eV, which correspond to the bonds of C–C/C=C, C—O and C═O respectively from graphene and/or phenyl (Ma et al., 2020). The O 1 s spectrum shows three peaks at 531.0, 532.1 and 532.6 eV, which are respectively attributed to lattice oxygen from Fe_3O_4, C–O/C=O and

Si–O–Si (Florek et al., 2020). The Fe 2p spectrum shows the peaks at 710.3, 712.9 and 724.5 eV, which are respectively attributed to Fe^{2+} $2p_{3/2}$, Fe^{3+} $2p_{3/2}$ and Fe $2p_{1/2}$ from Fe_3O_4. Above desirable composition and structural information confirm the successful construction of MG@mSiO_2-Phe.

The intensity of magnetization reflects the magnetic responsiveness of materials, that relates to the ability of separation from solution. Fig. 4E shows that Fe_3O_4, MRGO and MG@mSiO_2-Phe possess the specific saturation magnetization of 73.8, 39.4, 30.1 emu g^{-1}, respectively. Thus, the prepared MG@mSiO_2-Phe can be easily separated from sample solution. N_2 adsorption-desorption measurements were conducted to evaluate the specific surface area and characterize the pore size distribution of MG@mSiO_2-Phe. Fig. 4F shows the IV type curve with a sharp capillary condensation step at a relative pressure of 0.5. The BET surface area of MG@mSiO_2-Phe nanocomposites is 100.8 m^2 g^{-1}, and the average pore size calculated by Barrett-Joyner-Halenda (BJH) model is 3.83 nm (Fig. 4F, inset). The large surface area and abundant mesoporous structure are conducive to exposing functional groups (phenyl) for improving the adsorption capacity.

3.4. Feasibility of MSPE-DPV method for NFT determination

First, the adsorption behavior of MG@mSiO_2-Phe towards NFT was studied. The adsorption amounts were evaluated by determining the remaining NFT in solution by UV–Vis absorbance spectrometry after separation of MG@mSiO_2-Phe based on the established standard curve (Fig. S15, Supporting information). The adsorption kinetics of NFT by MG@mSiO_2-Phe was derived with varying contact time (1–50 min) as shown in Fig. S16 (Supporting information). The adsorption amounts gradually increase with the increasing contact time, and reach the maximal value after approximately 20 min. The experimental data were analyzed using the pseudo-first-order, pseudo-second-order and Weber-Morris kinetic models. It is found that the adsorption behavior of NFT by MG@mSiO_2-Phe closely follows the pseudo-second-order ($R^2 = 0.999$), rather than pseudo-first-order ($R^2 = 0.723$) or Weber-Morris ($R^2 = 0.629$) model, indicating the chemisorption contributes to the rate-determined step during the adsorption process (Zhang, Guo, et al., 2023). The effect of the different initial concentrations of NFT solution on the adsorption amounts of MG@mSiO_2-Phe was also evaluated (Fig. S17, Supporting information). The adsorption amounts gradually increase with the increase of NFT initial concentration and remain almost unchanged at 9.2 μg mg^{-1}. Two typical isotherm models (Langmuir and Freundlich) were fitted to evaluate the experiment data. The higher correlation coefficient ($R^2 = 0.997$) is observed in Langmuir fitting curve, suggesting that the adsorption of NFT by MG@mSiO_2-Phe coheres with Langmuir isotherm model based on the monolayer adsorption (Luo et al., 2024).

The electrode modification and NFT enrichment in the proposed MSPE-DPV determination method were investigated by CV and DPV (Fig. 5A and B). All CV results show a clear reduction peak at around −0.4 V, which is attributed to the reduction of the nitro group (–NO_2) to hydroxylamine derivative (–NHOH) in NFT molecule (Li et al., 2023). The electroreduction mechanism of NFT is illustrated in Fig. 5C. The curve a (Fig. 5A) acquired from immersing bare MGCE into 20 μmol L^{-1} NFT solution shows a weak reduction peak of NFT, and the curve b from bare MGCE detection of NFT after the enrichment by MG@mSiO_2-Phe shows an enhanced reduction peak. Meanwhile, the curve c acquired from immersing the Co_5/N-CNS-CNTs/MGCE into 20 μmol L^{-1} NFT solution presents enhanced reduction peak current with a lower peak potential compared with that from bare MGCE (curve a), which reveals the enhanced catalytic activity and fast electron transfer of Co_5/N-CNS-CNTs/MGCE towards NFT. Finally, the curve d, acquired from the detection of enriched NFT on the Co_5/N-CNS-CNTs/MGCE, presents enhanced peak current compared with both curves b and c. Furthermore, the DPV, a highly sensitive technique, was performed from 0 V to −0.8 V to investigate the reduction peak of NFT, and the curves a-d in Fig. 5B show a consistent trend with those in CV. These results demonstrate that the modification of Co_5/N-CNS-CNTs and the enrichment by MG@mSiO_2-Phe can synergistically enhance the reduction peak current of NFT, resulting in the elevated detection sensitivity.

3.5. Evaluation of analytical performance

3.5.1. Optimization of analytical parameters

Before assessing the effect of MSPE-DPV protocol for NFT determination, various analytical parameters were optimized to achieve the best NFT detection performance, including the pH of NFT sample solution, the type of electrocatalysts for modifying electrode, the dosage of MG@mSiO_2-Phe and the pH of electrolyte.

As shown in Fig. S18A (Supporting information), the adsorption amounts of MG@mSiO_2-Phe towards NFT maintain ~9.1 μg mg^{-1} from pH 5.0 to 7.0, while it gradually decreases following the increase of pH from 7.0 to 9.0. The adsorption of MG@mSiO_2-Phe towards NFT relies on the π-π interaction, as well as the hydrogen bonding interaction between –Si–OH on MG@mSiO_2-Phe surface with carbonyl and epoxy in NFT and the electrostatic interaction between negatively charged SiO_2 and protonated amino groups in NFT. Therefore, the pH does not have a significant effect on the adsorption amounts from pH 5.0 to 7.0, whereas higher pH can result in the dissolution of SiO_2 and the deprotonation of amino groups (pK_a of NFT is 7.55), and then the decrease of adsorption amounts of MG@mSiO_2-Phe towards NFT. At last, the NFT solution pH of 7.0 was applied as the optimized condition for the MSPE procedure.

Five types of electrocatalysts for modifying electrode were employed for the detection of 20 μmol L^{-1} NFT after the enrichment of MG@mSiO_2-Phe (Fig. S18B, Supporting information). Co_5/N-CNS-CNTs modified electrode generates the strongest peak current in DPV, which further indicate that Co_5/N-CNS-CNTs is the best electrocatalyst among the five electrocatalysts prepared for the modification of electrode in

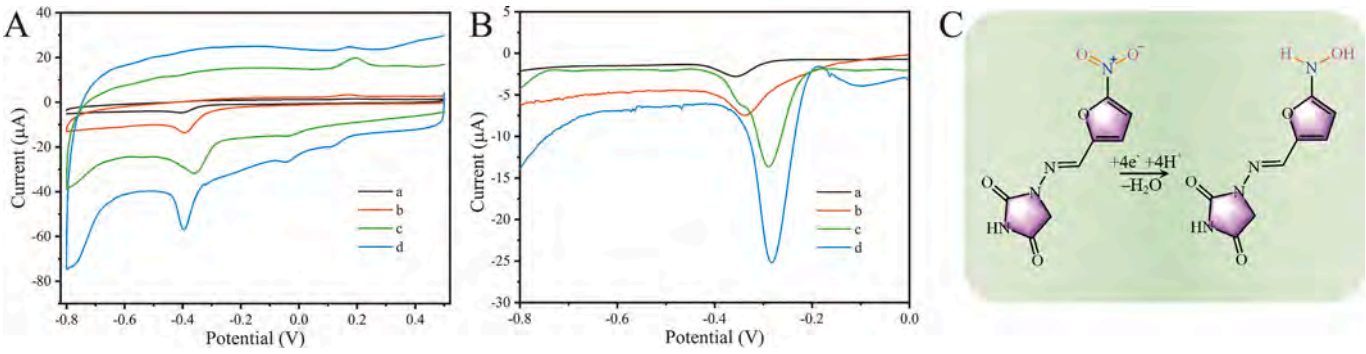

Fig. 5. (A) CV and (B) DPV recorded from different operating processes towards 20 μmol L^{-1} NFT, a: bare MGCE without MSPE, b: bare MGCE after MSPE, c: Co_5/N-CNS-CNTs/MGCE without MSPE and d: Co_5/N-CNS-CNTs/MGCE after MSPE. (C) The electroreduction mechanism of NFT.

NFT detection.

As shown in Fig. S18C (Supporting information), the peak current of DPV towards 20 μmol L^{-1} NFT gradually rises with the increase dosage of MG@mSiO$_2$-Phe from 0.05 to 0.25 mg, while the current begins to decrease from 0.25 mg. The bigger dosage of MG@mSiO$_2$-Phe means more adsorption active sites towards NFT, while excessive MG@mSiO$_2$-Phe can hinder the electron transport due to the non-conductivity of hybrid mesoporous silica in MG@mSiO$_2$-Phe. Thus, the MG@mSiO$_2$-Phe dosage of 0.25 mg was used in the MSPE of NFT.

As shown in Fig. S18D (Supporting information), the peak current of DPV towards 20 μmol L^{-1} NFT gradually rises with the increase of the electrolyte pH from 5.0 to 7.0, while the peak current begins to decrease from pH 7.0 to 9.0. This is attributed to the fact that the electrochemical reduction reaction of NFT involves protons (H^+), and the elevated pH leads to the lack of protons in the electrolyte medium (Li et al., 2023). Therefore, pH 7.0 was chosen as the optimized electrolyte pH for the DPV detection of NFT.

3.5.2. Analytical merits

Under the optimal experimental conditions, the DPV peak currents corresponding to different concentrations of NFT were measured after enrichment by MG@mSiO$_2$-Phe. In Fig. 6A, the DPV peak current I_p increases with the NFT concentration increasing from 0.05 to 250 μmol L^{-1}. The corresponding calibration plot exhibits good linearity between the I_p value and NFT concentration in two ranges of 0.05–20 μmol L^{-1} and 20–250 μmol L^{-1} (Fig. 6B), and their linear regression equations were fitted as I_p (μA) = 1.365 C_{NFT} (μmol L^{-1}) + 0.011 with R^2 = 0.991 and I_p (μA) = 0.271 C_{NFT} (μmol L^{-1}) + 21.624 with R^2 = 0.999, respectively. The limit of detection (LOD) was calculated to be 6 nmol L^{-1} using the formula: LOD = 3σ/S (σ represents the standard deviation of blank solution, n = 6, S represents the slope of the calibration curve). The key analytical characteristics were compared with the previously reported NFT determination methods as summarized in Table S1 (Supporting information). The results indicate that the proposed MSPE-DPV method for NFT determination has high sensitivity. Moreover, the matrix effect (ME) (Dai et al., 2023) was investigated to assess the degree of signal enhancement or suppression by matrix in cattle and sheep feed and skimmed milk, which is rarely mentioned in the other works listed in Table S1 (Supporting information). The MEs were respectively calculated as −19.1 % and − 11.0 % in feed and milk by analyzing the NFT standard curve and matrix-matched calibration curves (Fig. S19, Supporting information), which is considered that signal suppression is acceptable within ±20 %. For comparison, the MEs of direct DPV (−52.8 % and − 56.5 %) and SPE-HPLC (−11.7 % and − 5.2 %) methods in feed and milk, respectively, were also calculated and shown in Table S2 (Supporting information). The MSPE-DPV method possesses smaller MEs than the direct DPV detection, suggesting that the matrix interference is reduced by extracting NFT analytes from the matrices by MSPE like standard SPE-HPLC.

The anti-interference study is a key indicator to evaluate practical application of a determination method. 20 μmol L^{-1} NFT coupled respectively with excessive biological compounds co-existing in-vivo, nitro compounds structurally similar to NFT and other antibiotics was electrochemically detected after MG@mSiO$_2$-Phe based magnetic separation. The reduction peak currents at −0.28 V do not change significantly after adding 200 μmol L^{-1} glucose (Glu), ascorbic acid (AA) and glycine (Gly), 100 μmol L^{-1} Mtz, Cap, Flu and MNA, and 40 μmol L^{-1} Cip, Nlt, Amo, Otc, Nfz and Fzd (Fig. 6C), and the relative errors in the peak currents of the NFT mixed with interferents to that of standard NFT were calculated to be ≤10 % (Fig. 6D), indicating that the analytical protocol has a good anti-interference performance.

The reproduction quality of the electrodes was investigated by assaying 20 μmol L^{-1} NFT on eight batches of Co$_5$/N-CNS-CNTs modified electrodes under the same MSPE-DPV conditions. The slight changes of reduction peak currents (Fig. 6E) with the low relative standard deviation (RSD, 4.8 %) among the different modified electrodes are observed (Fig. S20, Supporting information), demonstrating the good batch-to-batch reproducibility of the prepared electrodes. Additionally, the stability of the protocol was investigated after storing the modified electrodes and MSPE material (MG@mSiO$_2$-Phe) for at

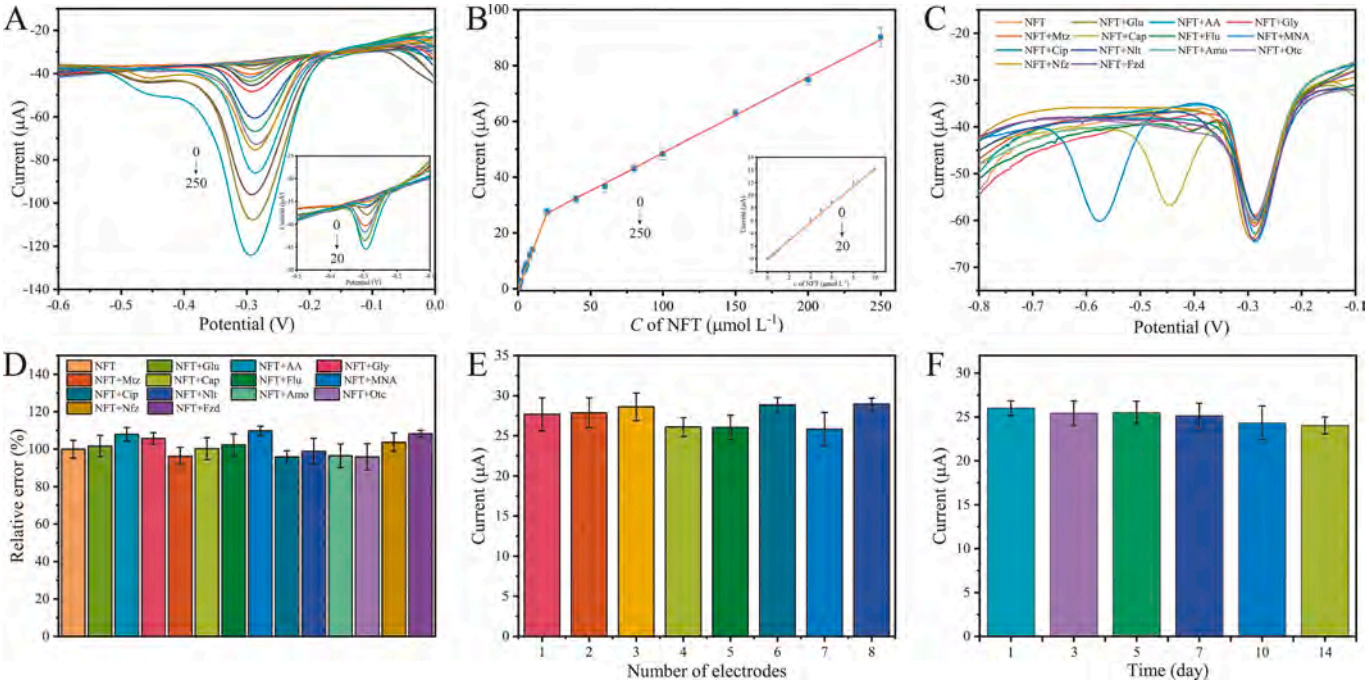

Fig. 6. (A) DPV responses at Co$_5$/N-CNS-CNTs/MGCE towards NFT of different concentrations in MSPE-DPV procedure and (B) corresponding calibration plot of NFT. (C) DPV responses for 20 μmol L^{-1} NFT coupled with excessive interferents in MSPE-DPV procedure and (D) corresponding histogram of relative errors. (E) The reproducibility analysis on eight batches of modified electrodes and (F) the storage stability analysis of modified electrodes and MSPE materials (MG@mSiO$_2$-Phe) towards 20 μmol L^{-1} NFT under the same MSPE-DPV conditions.

least two weeks. The reduction peak currents of 20 μmol L^{-1} NFT do not exhibit obvious weakening and remain 92.4 % of the original value after two weeks (Fig. 6F and S21, Supporting information), which indicates an acceptable long-term stability. The reusability of the MG@mSiO_2-Phe for NFT adsorption with Co_5/N-CNS-CNTs modified electrodes for NFT DPV detection was investigated. As shown in Fig. S22 (Supporting information), the NFT adsorption rate of MG@mSiO_2-Phe maintains over 87 % after five adsorption-desorption cycles, and the DPV peak current of NFT produced from a modified electrode remains 93.5 % of the initial value after eight detection-cleaning cycles. The results demonstrate the good reusability of MG@mSiO_2-Phe for adsorption and modified electrodes for DPV detection.

3.6. Practical application in actual samples

The freshly purchased feed and milk were examined by SPE-HPLC method prior to the spike recovery experiments to make sure that the blank samples do not contain NFT, which was confirmed by no peaks at retention time of 7.5 min (Fig. S23, Supporting information). Table 1 shows that the recoveries of NFT in feed and milk are between 93.5 % and 97.3 % and the RSDs are less than 5.9 % by the proposed MSPE-DPV. Notably, trichloroacetic acid and NaOH solutions were used in the pretreatment process of skimmed milk, causing the ionic system of sample solution different from that of the NFT standard solution. However, Fig. S24 (Supporting information) shows that the ionic type and strength have little effect on the adsorption of MG@mSiO_2-Phe towards NFT at the same pH. For the direct DPV detection, the recoveries are between 79.3 % and 82.8 %, and the RSDs are between 8.9 % and 12.6 %. For the SPE-HPLC method, the recoveries are between 90.5 % and 96.3 %, and the RSDs are between 1.3 % and 2.6 %. The MSPE-DPV method possesses higher recoveries and lower RSDs compared with direct DPV detection, and does not require matrix dilution. On the other hand, relative to SPE-HPLC method, the RSDs of the proposed protocol are somewhat higher, however, the recoveries are comparable. The results indicate that the MSPE-DPV method has strong anti-interference capability and detection accuracy as well as good reliability towards the NFT determination in complex matrix.

In the sample pretreatment procedure of feed and milk, SPE-HPLC method requires two evaporation/re-dissolution operation steps and six solutions through the SPE cartridge, and some instruments (nitrogen blower and air pump) are also essential. The sample pretreatment procedure is simplified in this proposed MSPE-DPV method, which requires only one evaporation/re-dissolution operation step, and the MSPE with MG@mSiO_2-Phe does not require any elution step. Moreover, the MSPE operation can be performed on the magnetic electrode without any additional devices even a magnet. The results of comparative analyses demonstrate that the MSPE-DPV protocol is suitable for reliable and rapid on-site NFT detection in actual samples.

4. Conclusion

A novel method integrating the MSPE pretreatment technology and DPV electrochemical detection was proposed for the NFT determination in complex cattle and sheep feed and skimmed milk samples. The constructed Co_5/N-CNS-CNTs catalysts showed hierarchical structure with abundant CNTs and Co-N_x active sites, which possessed excellent electrical conductivity and catalytic property towards electrochemical detection of NFT. The signal amplification by Co_5/N-CNS-CNTs electrocatalyst in couple with the analyte enrichment by MG@mSiO_2-Phe adsorbent can synergistically improve the sensitivity of NFT detection. Eventually, a wide linear range was achieved for NFT detection with low LOD. The proposed MSPE-DPV method was successfully applied in actual samples with excellent sensitivity, accuracy and reliability as well as acceptable MEs and satisfactory recoveries. The most attractive advantage is that, from the aspect of electrochemical detection, the introduction of MSPE by using MG@mSiO_2-Phe as the adsorbent allows electrochemical detection to be applied into complex samples without matrix dilution. Another one is that, from the aspect of sample pretreatment, the proposed MSPE-DPV method greatly simplifies sample pretreatment procedure compared with the traditional SPE-HPLC method. Moreover, the modified magnetic electrode plays the role of magnet so that the solvent elution even the solution transfer for the target analytes is no longer necessary in MSPE-electroanalytical procedures.

Table 1
Recoveries of NFT in cattle and sheep feed and skimmed milk samples by the proposed MSPE-DPV method, as well as direct DPV and SPE-HPLC methods.

Sample	Method	Added (μmol L^{-1})	Found (μmol L^{-1}, mean ± sd, $n \geq 3$)	Recovery (%)	RSD (%)
Feed	MSPE-DPV	0	nd[a]	–	–
		4	3.82 ± 0.17	95.5	4.5
		8	7.78 ± 0.32	97.3	4.0
		50	46.8 ± 2.7	93.5	5.7
		100	93.6 ± 5.5	93.6	5.9
	DPV	0	nd	–	–
		4	3.22 ± 0.38	80.5	11.7
		8	6.62 ± 0.68	82.8	10.2
	SPE-HPLC	0	nd	–	–
		4	3.62 ± 0.08	90.5	2.3
		8	7.61 ± 0.20	95.1	2.6
Milk	MSPE-DPV	0	nd	–	–
		4	3.82 ± 0.09	95.5	2.4
		8	7.64 ± 0.11	95.5	1.4
		50	48.5 ± 2.5	97.1	5.1
		100	94.1 ± 2.8	94.1	3.0
	DPV[b]	0	nd	–	–
		4	3.17 ± 0.39	79.3	12.6
		8	6.47 ± 0.58	80.9	8.9
	SPE-HPLC	0	nd	–	–
		4	3.85 ± 0.05	96.3	1.4
		8	7.69 ± 0.10	96.1	1.3

[a] nd = not detected. [b] 10-fold diluted matrix.

CRediT authorship contribution statement

Xingdong Yang: Writing – original draft, Visualization, Methodology, Investigation, Formal analysis. **Wan-yue Zhuang:** Visualization, Methodology, Investigation, Formal analysis. **Sen Zhang:** Visualization, Methodology, Investigation, Data curation. **Jie Zou:** Supervision, Methodology. **Aiguo Gu:** Resources, Funding acquisition. **Qi Wang:** Methodology, Formal analysis. **Jun-qin Qiao:** Resources, Funding acquisition. **Hong-zhen Lian:** Writing – review & editing, Supervision, Resources, Project administration, Funding acquisition, Conceptualization.

Declaration of competing interest

The authors declare that they have no known competing financial interests or personal relationships that could have appeared to influence the work reported in this paper.

Acknowledgments

This work was supported by the National Natural Science Foundation of China (22176085, 21874065 and 22304075), the National Key Research and Development Program of China (2021YFF0600800), and the Science and Technology Program of Jiangsu Provincial Administration for Market Regulation (KJ2024003).

Appendix A. Supplementary data

Supplementary data to this article can be found online at https://doi.org/10.1016/j.foodchem.2025.145901.

Data availability

Data will be made available on request.

References

Arancibia, V., Valderrama, M., Madariaga, A., Zúñiga, M. C., & Segura, R. (2003). Extraction of nitrofurantoin and its toxic metabolite from urine by supercritical fluids. Quantitation by high performance liquid chromatography with UV detection. *Talanta, 61*, 377–383. https://doi.org/10.1016/S0039-9140(03)00276-5

Chen, Y.-Z., Wang, C., Wu, Z.-Y., Xiong, Y., Xu, Q., Yu, S.-H., & Jiang, H.-L. (2015). From bimetallic metal-organic framework to porous carbon: High surface area and multicomponent active dopants for excellent electrocatalysis. *Advanced Materials, 27*, 5010–5016. https://doi.org/10.1002/adma.201502315

Dai, J., Lin, H., Pan, Y., Sun, Y., Wang, Y., Qiao, J.-Q., … Xu, C.-X. (2023). Determination of chlorpromazine and its metabolites in animal-derived foods using QuEChERS-based extraction, EMR-lipid cleanup, and UHPLC-Q-Orbitrap MS analysis. *Food Chemistry, 403*, Article 134298. https://doi.org/10.1016/j.foodchem.2022.134298

Dou, S., Li, X., Tao, L., Huo, J., & Wang, S. (2016). Cobalt nanoparticle-embedded carbon nanotube/porous carbon hybrid derived from MOF-encapsulated Co_3O_4 for oxygen electrocatalysis. *Chemical Communications, 52*, 9727–9730. https://doi.org/10.1039/C6CC05244D

Entry-Exit Inspection & Quarantine Industrial Standard of China. (2013). Determination of furazolidone, nitrofurantoin, furaltadone and nitrofurazone in animal feeding stuff - HPLC method. *SN/T*, 2013–2648. http://down.foodmate.net/standard/yulan.php?itemid=39525.

FDA Food Program Compendiun of Analytical Laboratory Methods. (2019). Determination of chloramphenicol and nitrofuran metabolites in cobia, croaker, and shrimp using microwave-assisted derivatization, automated SPE, and LC-MS/MS. C-011.01. https://www.fda.gov/media/131509/download.

Feng, J., She, X., He, X., Zhu, J., Li, Y., & Deng, C. (2018). Synthesis of magnetic graphene/mesoporous silica composites with boronic acid-functionalized pore-walls for selective and efficient residue analysis of aminoglycosides in milk. *Food Chemistry, 239*, 612–621. https://doi.org/10.1016/j.foodchem.2017.06.052

Florek, J., Larivière, D., Kählig, H., Fiorilli, S. L., Onida, B., Fontaine, F.-G., & Kleitz, F. (2020). Understanding selectivity of mesoporous silica-grafted diglycolamide-type ligands in the solid-phase extraction of rare earths. *ACS Applied Materials & Interfaces, 12*(51), 57003–57016. https://doi.org/10.1021/acsami.0c16282

Jeong, H.-K., Lee, Y. P., Lahaye, R. J. W. E., Park, M.-H., An, K. H., Kim, I. J., Yang, C.-W., Park, C. Y., Ruoff, R. S., & Lee, Y. H. (2008). Evidence of graphitic AB stacking order of graphite oxides. *Journal of the American Chemical Society, 130*, 1362–1366. https://doi.org/10.1021/ja076473o

Kaufmann, A., Butcher, P., Maden, K., Walker, S., & Widmer, M. (2015). Determination of nitrofuran and chloramphenicol residues by high resolution mass spectrometry versus tandem quadrupole mass spectrometry. *Analytica Chimica Acta, 862*, 41–52. https://doi.org/10.1016/j.aca.2014.12.036

Khong, S.-P., Gremaud, E., Richoz, J., Delatour, T., Guy, P. A., Stadler, R. H., & Mottier, P. (2004). Analysis of matrix-bound nitrofuran residues in worldwide-originated honeys by isotope dilution high-performance liquid chromatography-tandem mass spectrometry. *Journal of Agricultural and Food Chemistry, 52*(17), 5309–5315. https://doi.org/10.1021/jf0401118

Kokulnathan, T., & Chen, S.-M. (2020). Robust and selective electrochemical detection of antibiotic residues: The case of integrated lutetium vanadate/graphene sheets architectures. *Journal of Hazardous Materials, 384*, Article 121304. https://doi.org/10.1016/j.jhazmat.2019.121304

Li, M., Zhe, T., Li, R., Bai, F., Jia, P., Xu, Z., … Wang, L. (2023). ZIF-derived co nanoparticles embedded into *N*-doped carbon nanotube composites for highly efficient electrochemical detection of nitrofurantoin in food. *Food Chemistry, 418*, Article 135948. https://doi.org/10.1016/j.foodchem.2023.135948

Li, Z., Li, Z., & Xu, D. (2017). Simultaneous detection of four nitrofuran metabolites in honey by using a visualized microarray screen assay. *Food Chemistry, 221*, 1813–1821. https://doi.org/10.1016/j.foodchem.2016.10.099

Liu, W., Zhao, C., Zhang, Y., Lu, S., Liu, J., & Xi, R. (2007). Preparation of polyclonal antibodies to a derivative of 1-aminohydantoin (AHD) and development of an indirect competitive ELISA for the detection of nitrofurantoin residue in water. *Journal of Agricultural and Food Chemistry, 55*(17), 6829–6834. https://doi.org/10.1021/jf070620k

Liu, Z., Wang, J., Guo, Y., Liu, W., Yang, X., Wu, Q., & Wang, Z. (2022). Sensitive determination of auxins in environmental water and peach beverage by hyper crosslinked polymer-based solid-phase extraction with high performance liquid chromatography-fluorescence detection. *Journal of Chromatography. A, 1678*, Article 463345. https://doi.org/10.1016/j.chroma.2022.463345

Luo, R., Zhang, K., Qin, Y., Xie, L., Chai, X., Zhang, L., Du, G., Ge, S., Rezakazemi, M., Aminabhavi, T. M., & Xu, K. (2024). Amine-functionalized UiO-66 incorporated electrospun cellulose/chitosan porous nanofibrous membranes for removing copper ions. *Chemical Engineering Journal, 480*, Article 148077. https://doi.org/10.1016/j.cej.2023.148077

Ma, W., Wang, N., Fan, Y., Tong, T., Han, X., & Du, Y. (2018). Non-radical-dominated catalytic degradation of bisphenol A by ZIF-67 derived nitrogen-doped carbon nanotubes frameworks in the presence of peroxymonosulfate. *Chemical Engineering Journal, 336*, 721–731. https://doi.org/10.1016/j.cej.2017.11.164

Ma, X., Hao, R., Wang, Z., Xu, P., Luo, Y., & Zhao, Y. (2020). Nanoscale $CuFe_2O_4$ monodispersedly anchored on reduced graphene oxide as excellent peroxydisulfate catalyst for removal of gaseous elemental mercury. *Chemical Engineering Journal, 401*, Article 126101. https://doi.org/10.1016/j.cej.2020.126101

Ma, Y., Wang, Y., Xie, D., Gu, Y., Zhu, X., Zhang, H., … Zhao, H. (2018). Hierarchical MgFe-layered double hydroxide microsphere/graphene composite for simultaneous electrochemical determination of trace Pb(II) and Cd(II). *Chemical Engineering Journal, 347*, 953–962. https://doi.org/10.1016/j.cej.2018.04.172

Miao, L., Hu, L., Hong, Z., Mao, X., Yang, R., Qiao, Z., Wang, Y., Zhao, J., Gong, H., Chen, Y., Zhong, Y., Tan, J., Liu, J., Cai, W., Lin, Z., & Zhu, Z. (2025). A review of methods and research progress in the detection of nitrofuran metabolites in foods. *Microchemical Journal, 209*, Article 112900. https://doi.org/10.1016/j.microc.2025.112900

National Standard of China. (2008). Determination for the residues of furaltadone, nitrofurazone, nitrofurantoin and furazolidone metabolites in milk and milk powder - LC-MS-MS method. GB/T 22987–2008. http://down.foodmate.net/standard/yulan.php?itemid=21353.

Sivaraman, N., Duraisamy, V., Luciou, L., Saraswathyamma, B., Kumar, S. M. S., & Thangamuthu, R. (2023). *In-situ* construction of N and P doped hollow sphere carbon for electrochemical sensing of antibiotic drug from poultry sustenance. *Electrochimica Acta, 441*, Article 141773. https://doi.org/10.1016/j.electacta.2022.141773

Song, X., Guo, L., Liao, X., Liu, J., Sun, J., & Li, X. (2017). Hollow carbon nanopolyhedra for enhanced electrocatalysis via confined hierarchical porosity. *Small, 13*, 1700238. https://doi.org/10.1002/smll.201700238

Stahnke, H., Kittlaus, S., Kempe, G., & Alder, L. (2012). Reduction of matrix effects in liquid chromatography-electrospray ionization-mass spectrometry by dilution of the sample extracts: How much dilution is needed? *Analytical Chemistry, 84*(3), 1474–1482. https://doi.org/10.1021/ac202661j

Sun, T., Zang, W., Yan, H., Li, J., Zhang, Z., Bu, Y., Chen, W., Wang, J., Lu, J., & Su, C. (2021). Engineering the coordination environment of single cobalt atoms for efficient oxygen reduction and hydrogen evolution reactions. *ACS Catalysis, 11*(8), 4498–4509. https://doi.org/10.1021/acscatal.0c05577

The Ministry of Agriculture and Rural Affairs of China. (2019). List of Drugs and Other Compounds Prohibited for Use in Food Animals. Announcement No. 250.. http://www.moa.gov.cn/govpublic/xmsyj/202001/t20200106_6334375.htm.

Wang, Y.-L., Zhao, P.-Y., Liang, B.-L., Chen, K., & Wang, G.-S. (2023). Carbon nanotubes decorated co/C from ZIF-67/melamine as high efficient microwave absorbing material. *Carbon, 202*, 66–75. https://doi.org/10.1016/j.carbon.2022.10.043

Wang, Z., Peng, S., Hu, Y., Li, L., Yan, T., Yang, G., Ji, D., Srinivasan, M., Pan, Z., & Ramakrishna, S. (2017). Cobalt nanoparticles encapsulated in carbon nanotube-grafted nitrogen and sulfur co-doped multichannel carbon fibers as efficient bifunctional oxygen electrocatalysts. *Journal of Materials Chemistry A, 5*, 4949–4961. https://doi.org/10.1039/C6TA10291C

Xia, B. Y., Yan, Y., Li, N., Wu, H. B., Lou, X. W., & Wang, X. (2016). A metal-organic framework-derived bifunctional oxygen electrocatalyst. *Nature Energy, 1*, Article 15006. https://doi.org/10.1038/nenergy.2015.6

Xie, Z., Hu, Y., Chen, Y., Wu, G., Li, G., & Zhong, Q. (2023). Effective enrichment and detection of biphenol diglycidyl ether, novolac glycerol ether and their derivatives in canned food using a novel magnetic sulfonatocalix[6]arene covalent cross-linked polymer as the adsorbent. *Food Chemistry, 399*, Article 133918. https://doi.org/10.1016/j.foodchem.2022.133918

Yang, P., Chang, J. S., Wong, J. W., Zhang, K., Krynitsky, A. J., Bromirski, M., & Wang, J. (2015). Effect of sample dilution on matrix effects in pesticide analysis of several matrices by liquid chromatography-high-resolution mass spectrometry. *Journal of Agricultural and Food Chemistry, 63*(21), 5169–5177. https://doi.org/10.1021/jf505168v

Yang, X., Ying, S.-M., Zhang, S., Dai, J., Gao, W., Wang, T.-Q., Qiao, J.-Q., Lian, H.-Z., & Mao, L. (2024). $CoFe_2O_4$ decorated graphene/C_{18}-functionalized mesoporous silica nanocomposites prepared for magnetic enrichment and electrochemical detection of promethazine in beef. *Chinese Chemical Letters, 35*, Article 108674. https://doi.org/10.1016/j.cclet.2023.108674

Yu, Z., Huang, L., Zhang, Z., & Li, G. (2022). Magnetic $Ti_3C_2T_x/Fe_3O_4$/ag substrate for rapid quantification of trace sulfonamides in aquatic products by surface enhanced Raman spectroscopy. *Chinese Chemical Letters, 33*, 3853–3858. https://doi.org/10.1016/j.cclet.2021.10.045

Zhang, H., Lai, H., Wu, X., Li, G., & Hu, Y. (2020). $CoFe_2O_4$@HNTs/AuNPs substrate for rapid magnetic solid-phase extraction and efficient SERS detection of complex samples all-in-one. *Analytical Chemistry, 92*(6), 4607–4613. https://doi.org/10.1021/acs.analchem.0c00144

Zhang, L., Zhao, Y., Zhou, X., Liu, F., Zhang, Y., Huang, J., & Fang, Z. (2023). Preparation of rGO/NiO nanocomposites by AC and nanosecond pulsed DBD. *Carbon, 214*, Article 118377. https://doi.org/10.1016/j.carbon.2023.118377

Zhang, S., Li, J.-Y., Gao, W., Qiao, J.-Q., & Lian, H.-Z. (2023). Magnetic Ti_3C_2 MXene nanosheets prepared for enrichment of phosphopeptides. *ACS Applied Materials & Interfaces, 15*(13), 16505–16514. https://doi.org/10.1021/acsami.3c00848

Zhang, X., Zhu, M., Jiang, Y., Wang, X., Guo, Z., Shi, J., Zou, X., & Han, E. (2020). Simple electrochemical sensing for mercury ions in dairy product using optimal Cu^{2+}-based metal-organic frameworks as signal reporting. *Journal of Hazardous Materials, 400*, Article 123222. https://doi.org/10.1016/j.jhazmat.2020.123222

Zhang, Y., Guo, W., Liu, D., & Ding, Y. (2023). Tailoring abundant active-oxygen sites of Prussian blue analogues-derived adsorbents for highly efficient Yb(III) capture. *Journal of Hazardous Materials, 445*, Article 130457. https://doi.org/10.1016/j.jhazmat.2022.130457

Zhou, Q., Luo, L., Xia, L., Cha, C., Jiang, F., Wang, H., … Shu, L. (2023). Persulfate enhanced removal of bisphenol a by copper oxide/reduced graphene oxide foam:

Influencing factors, mechanism and degradation pathway. *Chemosphere, 340*, Article 139786. https://doi.org/10.1016/j.chemosphere.2023.139786

Zhu, M.-C., Lu, Y.-Z., Chen, S.-W., Hu, Z.-X., Wang, J.-W., Li, N., & Zeng, R. J.-X. (2023). Carbon nano-onions acting as artificial pili enhance chloramphenicol degradation in an anaerobic membrane bioreactor. *Chemical Engineering Journal, 475*, Article 146110. https://doi.org/10.1016/j.cej.2023.146110

Zhu, Y., Chandra, P., & Shim, Y.-B. (2013). Ultrasensitive and selective electrochemical diagnosis of breast cancer based on a hydrazine-au nanoparticle-aptamer bioconjugate. *Analytical Chemistry, 85*(2), 1058–1064. https://doi.org/10.1021/ac302923k